UC San Diego
UC San Diego Previously Published Works

Title

Built-In Active Microneedle Patch with Enhanced Autonomous Drug Delivery.

Permalink

https://escholarship.org/uc/item/3nq2f9h9

Journal

Advanced materials (Deerfield Beach, Fla.), 32(1)

ISSN

0935-9648

Authors

Lopez-Ramirez, Miguel Angel
Soto, Fernando
Wang, Chao
et al.

Publication Date

2020

DOI

10.1002/adma.201905740

Peer reviewed

Built-In Active Microneedle Patch with Enhanced Autonomous Drug Delivery

Miguel Angel Lopez-Ramirez[#],

Department of Nanoengineering, University of California San Diego, La Jolla, CA 92093, USA

Fernando Soto[#],

Department of Nanoengineering, University of California San Diego La Jolla, CA 92093, USA

Chao Wang,

Department of Nanoengineering, University of California San Diego La Jolla, CA 92093, USA

Ricardo Rueda,

Department of Nanoengineering, University of California San Diego, La Jolla, CA 92093, USA

Sourabh Shukla,

Department of Nanoengineering, University of California San Diego, La Jolla, CA 92093, USA

Cristian Silva-Lopez,

Department of Nanoengineering, University of California San Diego, La Jolla, CA 92093, USA

Daniel Kupor,

Department of Nanoengineering, University of California San Diego, La Jolla, CA 92093, USA

David A. McBride,

Department of Nanoengineering, University of California San Diego, La Jolla, CA 92093, USA

Chemical Engineering Program, University of California San Diego, La Jolla, San Diego, CA 92093, USA

Jonathan K. Pokorski [Prof],

Department of Nanoengineering, University of California San Diego, La Jolla, CA 92093, USA

Center for Nano-Immunoengineering, University of California San Diego, La Jolla, San Diego, CA 92093, USA

Amir Nourhani [Prof],

nsteinmetz@ucsd.edu; nshah@ucsd.edu;.

Department of Nanoengineering, University of California San Diego, La Jolla, CA 92093, USA

Nicole F. Steinmetz [Prof],
Center for Nano-Immunoengineering, University of California San Diego La Jolla, San Diego, CA 92093, USA

Department of Radiology, University of California, San Diego, La Jolla, San Diego, CA 92093, USA,

Department of Bioengineering, University of California, San Diego, La Jolla, San Diego, CA 92093, USA

Nisarg J. Shah [Prof],
Department of Nanoengineering, University of California San Diego, La Jolla, CA 92093, USA

Chemical Engineering Program, University of California San Diego, La Jolla, San Diego, CA 92093, USA

Program in Immunology, University of California San Diego, La Jolla, San Diego, CA 92093, USA

Joseph Wang [Prof]
Department of Nanoengineering, University of California San Diego, La Jolla, CA 92093, USA

Center for Nano-Immunoengineering, University of California San Diego, La Jolla, San Diego, CA 92093, USA

[#] These authors contributed equally to this work.

Abstract

The use of microneedles has facilitated the painless localized delivery of drugs across the skin. However, their efficacy has been limited by slow diffusion of molecules and often requires external triggers. Herein, an autonomous and degradable, active microneedle delivery platform is introduced, employing magnesium microparticles loaded within the microneedle patch, as the built-in engine for deeper and faster intradermal payload delivery. The magnesium particles react with the interstitial fluid, leading to an explosive-like rapid production of H_2 bubbles, providing thenecessary force to breach dermal barriers and enhance payload delivery. The release kinetics of active microneedles is evaluated in vitro by measuring the amount of IgG antibody (as a model drug) that passed through phantom tissue and a pigskin barrier. In vivo experiments using a B16F10 mouse melanoma model demonstrate that the active delivery of anti-CTLA-4 (a checkpoint inhibitor drug) results in greatly enhanced immune response. and significantly longer survival. Moreover, spatially resolved zones of active and passive microneedles allow a combinatorial rapid burst response along with slow, sustained release, respectively. Such versatile and effective autonomous dynamic microneedle delivery technology offers considerable promise for a wide range of therapeutic applications, toward a greatly enhanced outcome, convenience, and cost.

Keywords

3D printing; active drug delivery; magnesium microparticles; micromotors; microneedles; transdermal delivery

Current efforts and recent innovations on drug delivery platforms have the potential to enhance therapeutic efficacy. Although existing therapy modalities (e.g., oral delivery, needles) have addressed a variety of therapeutic delivery requirements, there are urgent needs to develop efficient local delivery platforms that can overcome the pain and fear from hypodermic injections,[1–3] and address the limited absorption associated with systemic pill-based delivery,[4,5] while maintaining cost-efficacy, convenience, and comfort. One promising route relies on the use of microneedles (MNs) toward painless and localized delivery of drugs across the skin.[6–8] For example, MNs have been approved by the Food and Drug Administration (FDA)[9] for delivery of vaccines and pharmaceutical through the epidermis in clinical setting.[10–12] Furthermore, this route offers autonomy and ease of use, as the therapeutic payload is released autonomously over prolonged periods, based on the material properties or by the inclusion of encapsulated smart drug-loaded particles.[13,14] Nevertheless, microneedles commonly rely on passive diffusion, which limits the penetration depth and distribution of the therapeutic ferent external stimuli have been employed to enhance the drug permeation through the epidermis. These external triggers include electroporation,[15,16] ultrasound,[17,18] light,[19–21] and temperature.[22,23] However, the requirement of external (often costly and bulky) equipment limits the widespread use of such triggered delivery to specialized centralized lab settings and restricts their use in field settings and remote locations. Future efforts are thus required to combine the advantages of both autonomous and active delivery into a single microneedle delivery platform, while reducing the time and costs necessary for achieving high therapeutic efficiency.

Here, we present a degradable active microneedle delivery platform, capable of generating autonomously vigorous convective fluid flows, for a greatly enhanced payload permeation (Figure 1). Our patch delivery system consists of a degradable polymeric microneedle array loaded with the therapeutic payload along with active motor-Magnesium (Mg) microparticles. Upon skin insertion, the microneedle polymeric matrix starts to dissolve, exposing the embedded Mg particles to react instantaneously with the surrounding interstitial biofluid, resulting in a rapid generation of hydrogen bubbles.[24] Such microbubble formation induces distinct vortex flow fields that lead to a powerful and autonomous "pumping-like" action and locally applied force, that results in a dynamic and extremely efficient transport and permeation of the embedded therapeutic payload.[25,26] The drug release kinetics of our active microneedle model was tested in vitro by measuring the amount of therapeutic payload that passed through tissue-mimicking phantom gel and pigskin barriers, demonstrating a greatly enhanced permeation and distribution when compared to common passive MN. The distinct delivery and therapeutic advantages of the active autonomous microneedle platform are demonstrated in a B16F10 mouse melanoma model where the active treatment led to a dramatically improved animal survival. The enhanced therapeutic index may be explained by the enhanced permeation of the therapeutic antibodies through the tumor (as demonstrated in an ex vivo model) therefore improving its distribution as well as changes (increase) in the tumor pH environment due to the hydrogen depletion of Mg particles. The versatility of our approach is also demonstrated by integrating spatially resolved active and passive microneedle zones in the same patch, toward combinatorial (fast and sustained) release delivery. Overall, the active MN delivery presented here offers an autonomous, biocompatible, and highly efficient alternative for

faster release kinetics of payloads through the skin, hence obviating the need of external activation (and related triggering equipment), potentially reducing the time necessary to achieve high therapeutic efficiency.

Figure 1a illustrates a schematic illustration of the active payload delivery MN patch. The active microneedle structure contains both the therapeutic payload and spherical Mg microparticles (50–100 μm) within a poly(vinylpyrrolidone) (PVP) polymer matrix (Figure 1a, left part); once the MN patch pierces the skin, the polymer MN tip starts to dissolve, exposing the Mg particle surface to the surrounding biological fluid. PVP was chosen as the polymer due to its hydrophilic and biocompatible properties,[27] widespread use in variety of biomedical applications, presenting low cytotoxicity and biodegradability.[28] The Mg particles thus start to react with the interstitial fluid, resulting in their dissolution and rapid production of H_2 bubbles. The generated bubbles induce distinct vortex flow fields at the localized application site, which results in greatly enhanced permeation and active transport of the loaded payload Figure 1a, right part. Figure 1b shows a 15×15 microneedle array, illustrating the efficient loading of multiple microneedles (400 μm diameter base and 850 μm height) that preserve a robust hard structure and a sharp stiff tip (less than 5 μm). The ability to load both active microparticles and therapeutic payload in a single needle is illustrated by the fluorescence and digital microscopy photographs shown in Figure 1b (zoom in), where the microneedles are loaded with Rh6G (red color) and Mg particles (black dots). An SEM image of a single active microneedle tip loaded with Mg particles is illustrated in Figure 1c, as well as an energy-dispersive X-ray (EDX) analysis of the entrapped Mg particles, clearly showing the embedded microparticles within the needle, protected by the polymeric matrix. The consistency in the dimensions of the individual tips of the MN array is further supported by the MN height profile, shown in Figure S1 (Supporting Information). The magnification of a single microneedle shows the close packing of the magnesium particles within the microneedle structure.

Active MNs were fabricated by a micromolding technique (Figure 1d),[29,30] briefly, the Mg microparticles were first infiltrated into the microneedle negative poly(dimethylsiloxane) (PDMS) mold, following by the addition of the therapeutic payload and the PVP polymer matrix (pH 10.5); the latter was allowed to dry overnight. The final patch was transferred to an adhesive base and stored at room temperature (25 °C). The active microneedle reacts quickly after getting in contact with fluids, as shown by the time-lapse microscopy images shown in Figure 1e (at 30 s intervals). These images illustrate the rapid dissolution and vigorous hydrogen generation of a single active MN tip, which leads to an explosive-like behavior and a fast dissolution within less than 60 s.

The active microneedle can load diverse cargo combinations. The loading capacity of the patch was calculated based on 66% of the volume of conical structures that can be loaded with spherical particles.[31] We estimate that our MN array, comprising a total of 225 MN tips, can load a total volume of ≈10.13 μL in their tips, and include additional cargo in the MN array base, thus providing tunable loading of different doses (Figure S2, Supporting Information). Measurement of the mechanical strength of the active MN under tensile compression (using the set-up of Figure 2a) displayed a fracture point of 500 mN per needle, corroborating its potential ability to pierce skin and scalability for in vivo applications

(Figure 2b). Previous reports indicate that the minimum force required to pierce skin efficiently is 45 mN. A safety factor calculation was determined as a result of the ratio of the failure force to the stablished minimum force for microneedle insertion. Our active microneedles have a safety factor number of 11, considerably higher than the minimum safety factor number of 2, which is considered adequate.[32] MN tips were also visualized by scanning electron microscopy (SEM) before and after the application of different loads (0.1, 0.25, and 0.5 N), where Mg particles can be seen inside the MN structure after fracturing.

We studied the dissolution of MNs containing different cargoes, including active particles, inert particles, and polymer only (Figure S3, Supporting Information). The MN dissolution rate changes significantly upon incorporating the active particles due to the H_2 bubble generation when compared to static particles and bare polymer MNs. The Mg reaction is primarily influenced by the pH of the biofluid solution and can increase the local pH after the microneedle dissolution; therefore, the hydrogen generation is directly related to the dissolution of Mg (Figure S4, Supporting Information). Low pH solutions (4 and 6) induced faster activation time and shorter life-time of single Mg particles, compared to neutral pH, which leads to slower activation of the particles and a longer lifetime. The pH of the biofluid has a direct effect on the mixing capabilities, with higher pH presenting faster hydrogen generation thus better mixing (Figure S5, Supporting Information). The pH range was selected on the basis of simulating transdermal pH. Commonly, normal tissue has an intracellular (pH_i) from ≈6.7 to 7.2 and extracellular (pH_e) of ≈7.3–7.4; as a universal characteristic of tumor microenvironment, solid tumors have demonstrated to have higher pH_i (7.1–7.6) and lower pH_e (6.2–6.9).[33] The hydrogen generation can be finally tuned by the addition of an enteric coating on the surface of the particles to delay their activation, as well as the inclusion of smaller Mg particles (<15 μm) within the MN structure; both studies are represented in Figures S6 and S7 (Supporting Information), respectively, and in Video S1 (Supporting Information). Such tunable actuation could result in tailored therapies and therapeutic modalities.

The reaction of the embedded Mg microparticles substantially increases the displacement of tracer microparticles through efficient localized fluid convection and mixing resulting from their hydrogen microbubbles production (Figure 2c). We measured the mean square displacement of fluorescent bead tracers (0.9 μm) by following their trajectories under the flow field generated by the Mg active particles and under Brownian motion (Figure 2d). The active particles present significantly higher mixing and hence greatly enhance the mass transport when compared to their static counterparts. Figure 2e, overlaps a stack of fluorescent microscopy images, visualizing the negligible flow generated in the absence of Mg particles (Brownian motion) as a control Figure 2e(i), and the flow lines generated with Mg particles Figure 2e(ii) (active).

The combined effect of faster MN dissolution and fluid mixing is shown in the time-lapse images of two microneedle tips without and with Mg particles (Figure 2f). It is clearly depicted that the vigorous localized mixing due to the embedded particles greatly accelerates the dissolution of the polymer due to their fast activation, but more notorious is the accelerated collision of the tracer particles in solution compared to passive MNs (as also illustrated in Video S2, Supporting Information). In addition, active MNs were loaded with

Rh6G, the resulting accelerated dissolution and Mg particle activity are shown in Video S3 (Supporting Information).

The accelerated and enhanced localized particle induced mixing was corroborated by a COMSOL Multiphysics simulation of the flow generated without and with particles, Figure 2g,i and 2g,ii, respectively, for the early stages of microneedle dissolution and activation. Upon reaction of Mg particles with the solution, gas bubbles nucleate and move upward due to buoyancy force. To obtain a simple picture and capture the essential physics of the problem, we approximated the effect of bubble motion by point forces F_i at the location of the ith bubble. While a rough approximation, the results provide a qualitative picture, consistent with experimental observations. The fluid field u obeys the Stokes equation

$$- \nabla p + \nabla^2 u = \sum_i F_i \tag{1}$$

$$\nabla \cdot u = 0 \tag{2}$$

where the summation is over the bubbles present in the fluid. As shown in Figure 2g, the effect of bubble motions, modeled by point-forces, leads to pumping effect in the fluid. Due to the confined geometry, the fluid follows a circular pattern, and results in enhanced mixing. A similar pattern is observed in the experimental set up (Video S2, Supporting Information) with tracer particles. Upon the motion of the bubbles, the tracer particles near the substrate move toward the active Mg particle, while near the top of the liquid surface, the particles move away from the center.

This section evaluates the in vitro payload release and the potential use of active-particle MN toward enhanced and accelerated permeation. The active MN release kinetics were evaluated by employing three different techniques: electrochemical, spectrophotometric, and fluorescence. Briefly, for the electrochemical measurements of the payload, the active MN were loaded with 50 μg of a tagged IgG-HRP; the IgG Ab was used as a model payload model, while its HRP tag facilitates the electrochemical detection that compared the release kinetics of diverse approaches. A schematic illustration of the electrochemical set up used for detecting the released payload is represented in Figure 3a, consisting on a phantom mimicking tissue (1.5 mm of thickness), a reservoir of phosphate buffered saline (PBS) solution pH 6, and a screen-printed carbon electrode. For the electrochemical detection of the Ab, an amperometric i–t curve technique was performed for this measurement as repetitive runs for a fixed period. The MN patch was placed over the 1.5 mm in thickness phantom mimicking tissue and further pierced; below the phantom tissue, a reservoir of 3,3′, 5,5′-Tetramethylbenzidine + H_2O_2 solution was placed for the detection of current changes over electrode (HRP coupled to the Ab). The corresponding amperometry curves at 30 min are shown in Figure S8 (Supporting Information). The release of Ab from active or passive diffusion MNs that went through phantom tissue can be seen in Figure 3b. The results in Figure 3c clearly depict an average 15 time fold advantage at the 15 min mark where passive diffusion presents a release percentage of $3.8 \pm 1.8\%$, while the active delivery results in $58.5 \pm 15.1\%$ release. Similarly, the active microneedles resulted in a threefold increased delivery at 20 min, with $29.3 \pm 13.8\%$ bare versus $94.1 \pm 5.8\%$ active. Active MNs were

loaded with IgG Alexa Fluor-555 in order to corroborate the enhanced payload distribution and permeation into phantom-mimicking tissue when compared to those of passive (diffusion-based) MN. Similar to the electrochemical measurements, the setup consisted of a phantom-mimicking tissue of a 1.5 mm thickness and pierced with an MN array. Figure S9 (Supporting Information) shows the corresponding absorbance spectra of IgG-Alexa Fluor-555 that passed through the phantom-mimicking tissue and measured at different time intervals (10, 20, and 30 min) using bare and active MNs.

In addition, the lateral diffusion of a FITC (fluorescein isothiocyanate) loaded MN was evaluated by measuring the permeation of the fluorescent molecule through the transparent 1.5 mm thick phantom tissue (visualized via top view fluorescence, Figure 3d). It should be noted that there was no significant background fluorescence signal from polymer microneedles without FITC in the control in Figure 3d(i). Furthermore, FITC-loaded active MNs were compared against passive MNs, where top view images taken at different time intervals (0, 5, 10, and 15 min) corroborate the accelerated diffusion of FITC significantly at the mark of 10 min, showing a larger radius of diffusion of the loaded dye due to Mg reactivity. The corresponding time-frame images are shown in Video S4 (Supporting Information).

Furthermore, an evaluation of the dye release performance of both passive and active microneedles was performed ex vivo using porcine skin. Figure 4a illustrates a digital photograph of an active microneedle array consisting of 49 microneedles loaded with the dye Rh6G, before piercing the porcine skin. The porcine skin was pretreated with glutaraldehyde before piercing with microneedles in order to characterize the piercing capabilities. A colored SEM image, shown in Figure 4b, clearly illustrates the successful penetration of two tips into deep tissue. The depth penetration results by piercing porcine skin with both passive and active microneedles were plotted and presented in Figure 4c. The penetration depth was plotted as a function of time, where the dye diffused across the skin from the microneedle structure. A schematic illustration of both passive and active microneedles piercing into porcine skin is illustrated in Figure 4d (left). The microneedle arrays were placed into a porcine skin rectangular area of 2 cm^2 and further examined at several time points (5, 10, and 20 min). Fluorescence cross section time-lapse images, illustrating the microneedle distribution inside the porcine skin models, are shown in Figure 4d (right). It should be noted that microneedles needed to contact the skin for at least 5 min to fully dissolve and deliver the payload. These data indicate that the entrapped Mg particles greatly enhanced the delivery of the model dye Rh6G payload by lateral and vertical routes, versus the delayed delivery by passive microneedles, which starts at the 5 min mark. Such improved permeation and hence delivery is dramatically more pronounced at 10 min, where passive MNs lead to an average value of 111 ± 79 µm versus the 526 ± 71 µm value observed with the active microneedles.

The in vivo therapeutic efficacy of the active transport method was evaluated using a syngeneic and orthotopic mouse model of melanoma; specifically, B16F10 cells were grown dermally using C57Bl6 mice. We chose to test the active versus passive delivery of checkpoint blockade antibody anti-CTLA-4 (Clone: 9H10, BioXcel). Anti-CTLA4 checkpoint blockade is an immunotherapy approved by the FDA for the treatment of

melanoma since 2011 and is in clinical trials targeting other solid tumors.[34,35] Additionally, anti-CTLA4 has been recognized to be a susceptible therapy in B16F10 melanoma model. [36] On days 10 and 17 post-tumor challenge, various treatment groups were administered intratumorally; PBS control versus free anti-CTLA4 versus passive MN versus active MN (Figure 5a). For both MN experiments, the patches were applied manually into the mice right flank for 15 min. The efficacy was assessed by measuring the tumor growth rate and survival. As expected, free anti-CTLA-4 Ab treatment delayed tumor growth compared to untreated animals (PBS control group). However, both the passive MN and active MN showed significantly enhanced antitumoral effects, achieving substantial tumor suppression (Figure 5b,c, respectively). Passive MN delivering the therapeutic anti-CTLA-4 Ab significantly delayed tumor growth; nevertheless, by day 46 all animals in this group had to be sacrificed due to tumor burden exceeding 1500 mm^3. In stark contrast, 60% of the animals treated using the active delivery MN platform showed a complete response and were tumor-free and survived past day 60 (Figure 5d). The corresponding blank active microneedle control is shown in Figure S10 (Supporting Information). We hypothesize that the dramatically improved efficacy is due to the active delivery mechanism. Based on the aforementioned ex vivo data, we hypothesize that the burst "fast" release mechanism of action, with built-in pumping action associated with the embedded Mg motors can be helpful in enhancing the permeation of anti-CTLA through the tumor, therefore improving its distribution as achieved in previous ex vivo model. Furthermore we hypothesize that changes (i.e., increase) in the tumor pH environment by the hydrogen depletion of Mg particles is also expected to contribute to enhancing the therapeutic effect, as it has been reported by the delivery of immune checkpoint inhibitors and alkalization agents.[37,38] Additionally, the active delivery mechanism is a promising therapy modality with a synergistic effect, acting as a pump to enhance the permeation of the payload and results in the intratumoral production of localized microbubbles (hydrogen therapy), that lead to antitumoral effects,[39,40] We evaluated the safety of the materials used in the active microneedle (Mg and PVP) and their subsequent by products (magnesium hydroxide), by performing toxicity studies in mice.

Analysis of the kidney, liver, lung, and spleen indicated no apparent systemic toxicities associated with the active or passive MN treatment (Figure S11, Supporting Information).

Finally, we illustrate how to integrate the active and combinatorial delivery platforms as a complement to existing microneedle designs that are commonly based on passive delivery by creating spatially resolved active and passive microneedle zones onto a single patch toward fast/deep and slow sustained delivery, respectively. The patch was fabricated by using a stereolithography 3D printer to generate a positive microneedle mold in which we engineered topological barriers (walls) to spatially separate the active and passive microneedle groups into different sections, thus allowing to combine different materials and cargoes in the same patch design (Figure 6a). A digital photograph and SEM images of the positive micromold (Figure 6b) clearly show in detail the distinct grooves that separate the microneedles into different subsections. SEM images illustrate in more detail the uniform spacing between such sections, and reproducible tip sharpness. Next, PDMS negative microneedle molds were fabricated and used to fabricate the combinatorial patch following the micromolding method described earlier but with the added capability of casting different

polymers and cargo in each of the microneedle compartments Figure 6c. Further details of the fabrication process are given in Figure S12 (Supporting Information).

An SEM image of the polymeric combinatorial MN patch is shown in Figure 6d, where both passive and active microneedle rows are side by side. The corresponding EDX analysis clearly indicates that the Mg particles are present only in the active compartment. For better visualization, we loaded each compartment with model fluorescent dye payloads. The passive MN compartment was loaded with FITC and the active compartment with Rh6G. Such combinatorial loading of both dyes in a single microneedle patch is further illustrated in Figure 6e, which shows a digital photograph of the dual compartment under UV light illumination. The dual MN patch was characterized by fluorescence microscopy, where a side-by-side image shows the spatially resolved MNs loaded with the different (dye) cargo (Figure 6f). To visualize the different activity of the MN tips, Figure 6g,h illustrates fluorescence time-lapse images, showing the dissolution of passive and active microneedles, where the active microneedle compartment dissolves and releases Rh6G with the burst activation of Mg particles, and passive microneedles release the second cargo (FITC) at a slower rate of delivery. Our combinatorial approach can overcome the challenge of loading and delivering fast and slow multiple cargos as a single treatment administration with a microneedle dissolvable patch. The different microneedles in such combinatorial array can thus be tailored to present different release kinetics based on the materials used in fabrication, were ideally a burst-sustained release profile could help to enhance the low efficiency of current passive transdermal treatments.

We have demonstrated an effective microneedle delivery route that offers active payload delivery, without the use of external stimuli, toward improved therapeutic outcome versus commonly used passive diffusive microneedle transport. Such active, degradable, and autonomous microneedle delivery has been realized through the incorporation of reactive Mg microparticles within the microneedle patch. The dissolution of these Mg particles (upon contact with the interstitial fluid) produces a remarkably high localized fluidic flow that results in a significantly faster and deeper intradermal local payload delivery. Such autonomous built-in mixing effect obviates the need for expensive and bulky external systems commonly used for triggering active MN delivery. Our methodology allowed the fabrication of a microneedle patch as well for combinatorial delivery using spatially resolved active and passive microneedle zones, for fast/deep and slow sustained release, respectively. The therapeutic advantages of such active transport were demonstrated from the greatly enhanced in vivo efficacy observed using a syngeneic and orthotopic mouse model of melanoma. In future work we plan to further study the immunological profile to fully delineate the mechanism of this therapy modality. Moreover, the active MN delivery system is not limited to specific polymeric materials or microneedle geometry or dimensions. The new "built-in" active delivery strategy holds considerable promise for diverse practical biomedical applications for transdermal delivery, including drug delivery, immunotherapy, or cosmetic treatment, offering an attractive efficient delivery route compared to traditional passive microneedle patches, as well as being an ideal candidate to particularly benefit applications, such as pain killing and cardiac treatment, that require fast and deep payload delivery.

Supplementary Material

Refer to Web version on PubMed Central for supplementary material.

Acknowledgements

References

[1]. Hickling JK, Jones KR, Friede M, Zehrung D, Chen D, Kristensen D, Bull. W. H. O. 2011, 89, 221. [PubMed: 21379418]

[2]. Drucker E, Alcabes PG, Marx PA, Lancet 2001, 358, 1989. [PubMed: 11747942]

[3]. Taddio A, Ipp M, Thivakaran S, Jamal A, Parikh C, Smart S, Sovran J, Stephens D, Katz J, Vaccine 2012, 30, 4807. [PubMed: 22617633]

[4]. Park K, Kwon IC, Park K, React. Funct. Polym. 2011, 71, 280.

[5]. Thanki K, Gangwal RP, Sangamwar AT, Jain S, Controlled Release J 2013, 170, 15.

[6]. GhavamiNejad A, Li J, Lu B, Zhou L, Lam L, Giacca A, Wu XY, Adv. Mater. 2019, 31, 1901051.

[7]. Kim YC, Park JH, Prausnitz MR, Adv. Drug Delivery Rev. 2012, 64, 1547.

[8]. Wang J, Wang Z, Yu J, Kahkoska AR, Buse JB, Gu Z, Adv. Mater. 2019, 17, 1902004.

[9]. Bhatnagar S, Dave K, Venuganti VVK, Controlled Release J 2017, 260, 164.

[10]. Sullivan SP, Koutsonanos DG, del Pilar Martin M, Lee JW, Zarnitsyn V, Choi SO, Murthy N, Compans RW, Skountzou I, Prausnitz MR, Nat. Med. 2010, 16, 915. [PubMed: 20639891]

[11]. DeMuth PC, Min Y, Huang B, Kramer JA, Miller AD, Barouch DH, Hammond PT, Irvine DJ, Nat. Mater. 2013, 12, 367. [PubMed: 23353628]

[12]. DeMuth PC, Moon JJ, Suh H, Hammond PT, Irvine DJ, ACS Nano 2012, 6, 8041. [PubMed: 22920601]

[13]. Yu J, Zhang Y, Ye Y, DiSanto R, Sun W, Ranson D, Ligler FS, Buse JB, Gu Z, Proc. Natl. Acad. Sci. USA 2015, 112, 8260. [PubMed: 26100900]

[14]. Ye Y, Yu J, Wang C, Nguyen NY, Walker GM, Buse JB, Gu Z, Adv. Mater. 2016, 28, 3115. [PubMed: 26928976]

[15]. Denet AR, Vanbever R, Préat V, Adv. Drug Delivery Rev. 2004, 56, 659.

[16]. Choi SO, Kim YC, Park JH, Hutcheson J, Gill HS, Yoon YK, Prausnitz MR, Allen MG, Biomed. Microdevices 2010, 12, 263. [PubMed: 20012696]

[17]. Mitragotri S, Blankschtein D, Langer R, Science 1995, 269, 850. [PubMed: 7638603]

[18]. Soto F, Jeerapan I, Silva-López C, Lopez-Ramirez MA, Chai I, Xiaolong L, Lv J, Kurniawan JF, Martin I, Chakravarthy K, Wang J, Small 2018, 14, 1803266.

[19]. Chen MC, Lin ZW, Ling MH, ACS Nano 2016, 10, 93. [PubMed: 26592739]

[20]. Dong L, Li Y, Li Z, Xu N, Liu P, Du H, Zhang Y, Huang Y, Zhu J, Ren G, Xie J, ACS Appl. Mater. Interfaces 2018, 10, 9247. [PubMed: 29493217]

[21]. Xie X, Pascual C, Lieu C, Oh S, Wang J, Zou B, Xie J, Li Z, Xie J, Yeomans DC, Wu MX, ACS Nano 2017, 11, 395. [PubMed: 28001346]

[22]. Lee H, Choi TK, Lee YB, Cho HR, Ghaffari R, Wang L, Choi HJ, Chung TD, Lu N, Hyeon T, Choi SH, Nat. Nanotechnol. 2016, 11, 566. [PubMed: 26999482]

[23]. Lee H, Song C, Hong YS, Kim MS, Cho HR, Kang T, Shin K, Choi SH, Hyeon T, Kim DH, Sci. Adv. 2017, 3, e1601314.

[24]. Esteban-Fernández de Ávila B, Angsantikul P, Li J, Lopez-Ramirez MA, Ramírez-Herrera DE, Thamphiwatana S, Chen C, Delezuk J, Samakapiruk R, Ramez V, Obonyo M, Zhang L, Wang J, Nat. Commun. 2017, 8, 272. [PubMed: 28814725]

[25]. Orozco J, Cheng G, Vilela D, Sattayasamitsathit S, Vazquez-Duhalt R, Valdes-Ramírez G, Pak OS, Escarpa A, Kan C, Wang J, Angew. Chem., Int. Ed. 2013, 52, 13276.

[26]. Wu Z, Li J, Esteban-Fernández de Ávila B, Li T, Gao W, He Q, Zhang L, Wang J, Adv. Funct. Mater. 2015, 25, 7497.

[27]. S. R. Montezuma, J. Loewenstein, C. Scholz, J. F. I. Rizzo, Invest. Opthalmol. Vis. Sci. 2006, 47, 3514.

[28]. Abd El-Mohdy H, Ghanem S, J. Polym. Res. 2009, 16, 1.

[29]. Li W, Terry RN, Tang J, Feng MR, Schwendeman SP, Prausnitz MR, Nat. Biomed. Eng. 2019, 3, 220. [PubMed: 30948808]

[30]. Lahiji SF, Kim Y, Kang G, Kim S, Lee S, Jung H, Sci. Rep. 2019, 9, 7886. [PubMed: 31133711]

[31]. Li S, Zhao J, Lu P, Xie Y, Chin. Sci. Bull. 2010, 55, 114.

[32]. Park JH, Allen MG, Prausnitz MR, Pharm. Res. 2006, 23, 1008. [PubMed: 16715391]

[33]. Wang L, Fan Z, Zhang J, Changyi Y, Huang C, Gu Y, Xu Z, Tang Z, Lu W, Wei X, Li C, Int. J. Cancer 2015, 136, E107.

[34]. Lipson EJ, Drake CG, Clin. Cancer Res. 2011, 17, 6958. [PubMed: 21900389]

[35]. Kvistborg P, Philips D, Kelderman S, Hageman L, Ottensmeier C, Joseph-Pietras D, Welters MJ, van der Burg S, Kapiteijn E, Michielin O, Romano E, Sci. Transl. Med. 2014, 6, 254ra128.

[36]. Curran MA, Montalvo W, Yagita H, Allison JP, Proc. Natl. Acad. Sci. USA 2010, 107, 4275. [PubMed: 20160101]

[37]. Pilon-Thomas S, Kodumudi KN, El-Kenawi AE, Russell S, Weber AM, Luddy K, Damaghi M, Wojtkowiak JW, Mulé JJ, Ibrahim-Hashim A, Gillies RJ, Cancer Res. 2016, 76, 1381. [PubMed: 26719539]

[38]. Li J, Angsantikul P, Liu W, Esteban-Fernández de Ávila B, Thamphiwatana S, Xu M, Sandraz E, Wang X, Delezuk J, Gao W, Zhang L, Wang J, Angew. Chem., Int. Ed. 2017, 56, 2156.

[39]. Wu Y, Yuan M, Song J, Chen X, Yang H, ACS Nano 2019, 13, 8505. [PubMed: 31329427]

[40]. Zandi A, Khayamian MA, Saghafi M, Shalileh S, Katebi P, Assadi S, Gilani A, Parizi MS, Vanaei S, Esmailinejad MR, Abbasvandi F, Adv. Healthcare Mater. 2019, 8, 1900613.
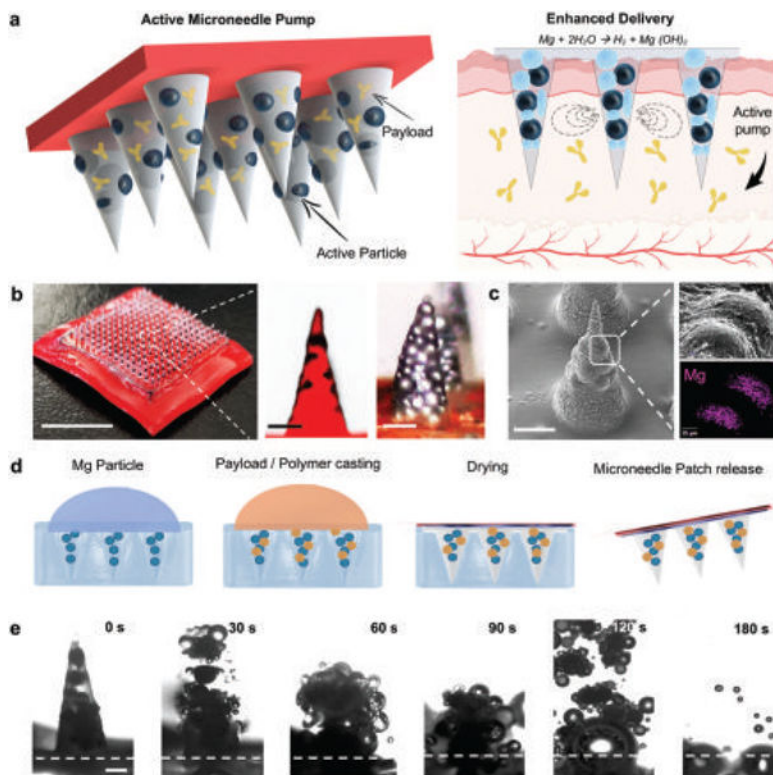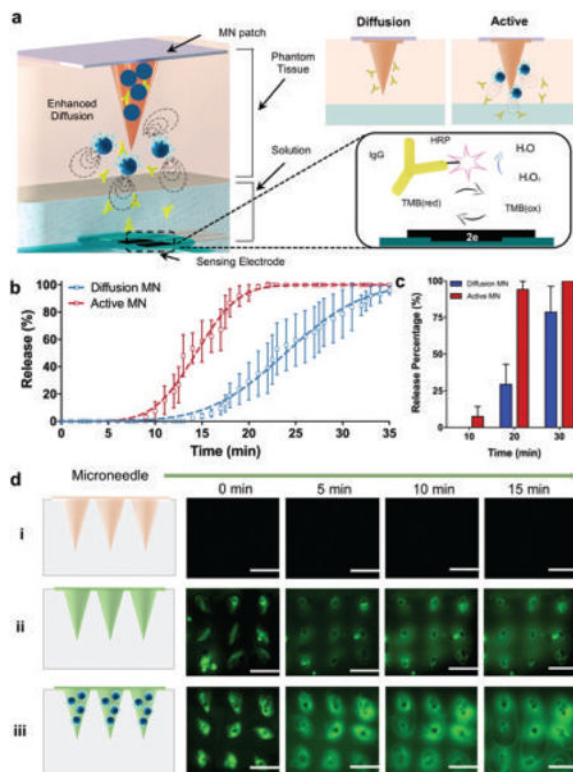
Figure 1.
Active microneedle for enhanced drug delivery. a) Active microneedle patch composition, and built-in Mg particle activation as pumps when in contact with bodily fluids, leading to an enhanced drug release. b) Digital photograph showing a patch of 15×15 microneedle array and optical/fluorescent microscopy images of an active MN tip loaded with Mg particles, scale bars, 6 mm and 200 μm, respectively. c) SEM image of single active microneedle tip and EDX analysis for Mg. Scale bars, 300 μm, and 25 μm, respectively. d) Fabrication steps of the microneedle patch: PDMS micromolding over master microneedle, PDMS negative MN mold released, Mg particle loading, polymer and payload inclusion, polymer drying, adhesive application and peel off. e) Microscopy time-frame images taken from a single active microneedle tip clearly showing polymer dissolution in PBS pH 6.0 and particle activation (30 s intervals), scale bar, 200 μm.
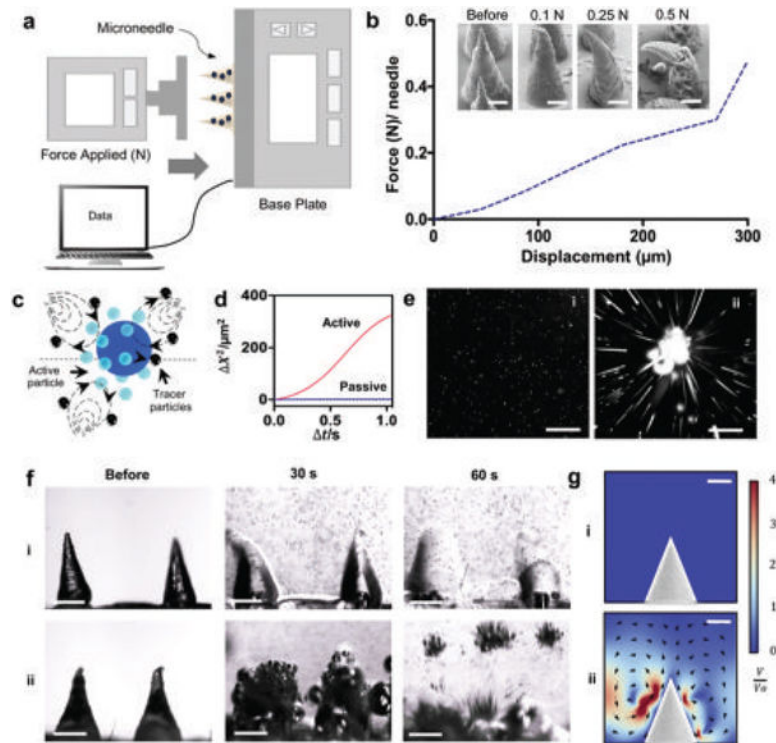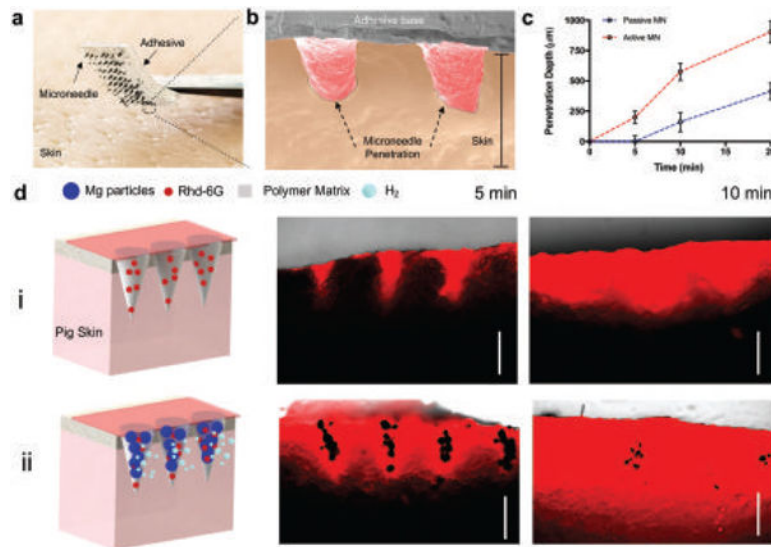
Figure 2.
Mechanical testing of the microneedle patch and active fluid transport (localized streaming) based on Mg particles embedded in dissolvable microneedles. a) Schematic illustration of the mechanical setup used. b) Mechanical analysis of a single microneedle tip under different loads and SEM images of microneedle tips before and after application of each load. Scale bars, 200 μm. c) Schematic of the fluid transport of active Mg particles in the presence of tracer particles. d) Mean square displacement of tracer particles using Brownian motion as control or in the presence of the active Mg particles at pH 6.0. Scale bar, 100 μm. e) Flow trace images of the trajectory (over 1s) of 0.9 μm polystyrene tracer particles at pH 6.0 without the presence of active particles (Brownian motion) (i), and with active particles (ii) at pH 6.0. Scale bars, 100 μm. f) Time-lapse images of two microneedle tips without active particles, showing the dissolution in PBS pH 6.0 of the transient polymer by diffusion (i) and with the Mg particles accelerating the dissolution of the transient polymer due to their fast activation (ii). Scale bars, 400 μm. g) COMSOL Multiphysics simulation of the flow generated by the absence (i) and presence (ii) of Mg particles within the MN structure.
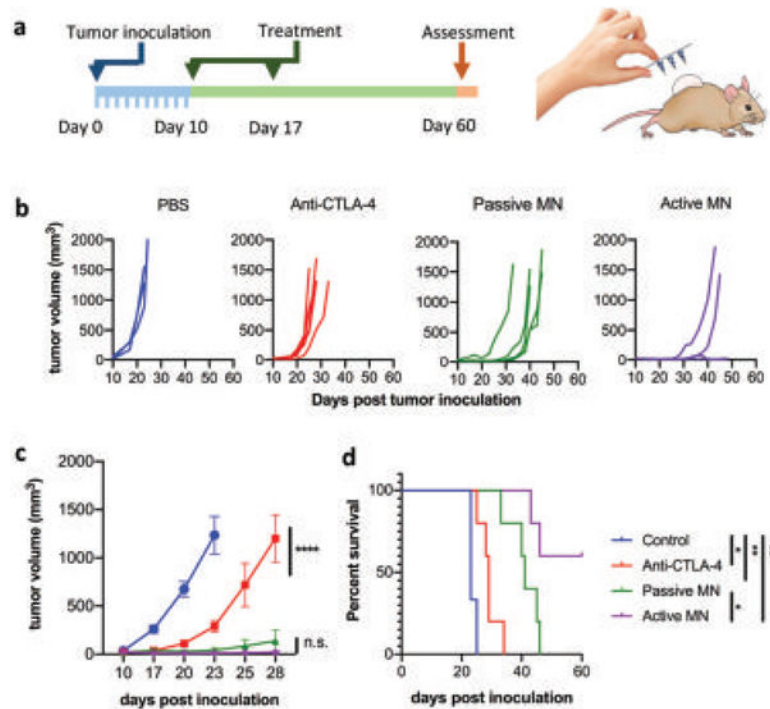
Figure 3.
Evaluation of the in vitro payload release performance of common passive and active microneedles by fluorescence, electrochemical, and spectrophotometric techniques. a) Schematic illustrating the electrochemical set up of the Ab-based amperometric detection. b) Release kinetics of corresponding Ab delivery of both passive and active MNs at pH 6.0. Passive MNs (PVP and IgG-HRP) and active microneedles (PVP, IgG-HRP, and Mg particles); $n = 5$. c) Corresponding release percentage of Ab at different time points; $n = 5$. d) Time-lapse fluorescence images (top view) of microneedles placed on top of a 1.5 mm phantom tissue, obtained at different time points (0–15 min). Blank unloaded MNs (i), FITC-loaded MNs (ii), and FITC-loaded active MNs (iii). Scale bar, 1 mm.
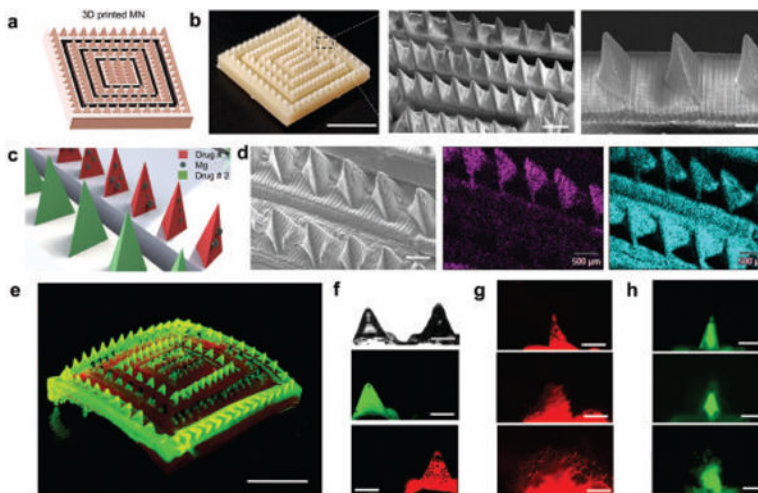
Figure 4.
Evaluation of ex vivo dye release performance of passive and active microneedles. a) Digital photograph of an active microneedle patch (7×7 array) loaded with Rh6G before piercing porcine skin. b) Colored SEM image of 2 active microneedles piercing porcine skin. Scale bar, 1 mm. c) Corresponding penetration depth of Rh6G by microneedles at different time points, $n = 3$. d) Schematic illustrating the experimental set up of both passive and active microneedles penetrating into porcine skin. Passive (i) and active (ii) microneedle arrays are shown, along with fluorescence microscopy cross-section images at different times. Scale bars, 500 μm.

Figure 5.
In vivo melanoma tumor eradication by active microneedles. a) In vivo skin-cancer treatment using anti-CTLA-4 antibodies delivered by active versus passive microneedles and intratumoral injection in the B16F10 dermal melanoma model. b) Tumor volumes growth curve of individual mice and averaged tumor volumes of mice receiving PBS (blue), free anti-CTLA-4 (red), anti-CTLA-4 passive microneedle (MN, green), and anti-CLTA-4 active MN (purple). Data are means ± SEM ($n = 3–5$). c) Tumor growth over time was compared by two-way ANOVA with Tukey's test: ****$p < 0.0001$, n.s. no significant difference. d) Survival rates. Statistical significance was calculated using Log-rank (Mantel–Cox) test: *$p < 0.05$, **$p < 0.01$.

Figure 6.
Combinatorial drug microneedle patch for the simultaneous dual delivery of different payloads. a) Schematic of square microneedle arrays as different active and passive compartments. b) Digital photograph of a 3D printed microneedle array by stereolithography and SEM images of needle rows with equal spacing. Scale bars, 5 mm, 1 mm, and 500 µm respectively. c) Schematic of a combinatorial dissolvable microneedle patch with two different microneedle compartments (active and passive). d) Side-by-side SEM image of active and passive microneedles along with the corresponding EDX images illustrating the Mg in magenta, and C in cyan. Scale bars, 500 µm. e) Digital photograph of a combinatorial dissolvable microneedle patch loaded with FITC (passive delivery compartment) and Rh6G + Mg particles (active delivery compartment). Scale bar, 5 mm. f) Side-by-side optical and fluorescence microscopy images showing active and passive microneedles. Scale bars, 500 µm. g) Fluorescence time-lapse images show the dissolution of an active microneedle tip at 10 s intervals. Scale bars, 500 µm. h) Fluorescence time-lapse images showing the dissolution of a passive microneedle tip. Scale bars, 500 µm.